



This is a repository copy of *Crystallisation of a simulated borosilicate high-level waste glass produced on a full-scale vitrification line*.

White Rose Research Online URL for this paper:
<http://eprints.whiterose.ac.uk/152454/>

Version: Accepted Version

Article:

Rose, P.B., Woodward, D.I., Ojovan, M.I. et al. (2 more authors) (2011) Crystallisation of a simulated borosilicate high-level waste glass produced on a full-scale vitrification line. *Journal of Non-Crystalline Solids*, 357 (15). pp. 2989-3001. ISSN 0022-3093

<https://doi.org/10.1016/j.jnoncrysol.2011.04.003>

Article available under the terms of the CC-BY-NC-ND licence
(<https://creativecommons.org/licenses/by-nc-nd/4.0/>).

Reuse

This article is distributed under the terms of the Creative Commons Attribution-NonCommercial-NoDerivs (CC BY-NC-ND) licence. This licence only allows you to download this work and share it with others as long as you credit the authors, but you can't change the article in any way or use it commercially. More information and the full terms of the licence here: <https://creativecommons.org/licenses/>

Takedown

If you consider content in White Rose Research Online to be in breach of UK law, please notify us by emailing eprints@whiterose.ac.uk including the URL of the record and the reason for the withdrawal request.



eprints@whiterose.ac.uk
<https://eprints.whiterose.ac.uk/>

Crystallisation of a simulated borosilicate high-level waste glass produced on a full-scale vitrification line

Peter B. Rose ^a, David I. Woodward ^b, Michael I. Ojovan ^a, Neil C. Hyatt ^a, William E. Lee ^{c,*}

^a *Immobilisation Science Laboratory, Department of Engineering Materials, University of Sheffield, Sheffield S1 3JD, UK*

^b *ITM Power plc, Sheffield Airport Business Park, Sheffield S9 1XU, UK*

^c *Department of Materials, Imperial College London, London SW7 2AZ, UK*

* Corresponding author. Tel.: +44 (0)20 7594 6733; fax: +44 (0)20 7594 6736. *E-mail address:* w.e.lee@imperial.ac.uk (W.E. Lee).

Abstract

A simulated (inactive) borosilicate high-level waste (HLW) glass was produced on a full-scale vitrification line with composition simulating vitrified oxide fuel (UO₂) reprocessing waste. As-cast samples were compositionally homogeneous (Type I microstructure) and/or compositionally inhomogeneous displaying compositional ‘banding’ and frequently containing ‘reprecipitated calcine’ (Type II microstructure). Crystal phases identified in as-cast samples were: tetragonal RuO₂, cubic Pd–Te alloy, cubic (Cr,Fe,Ni,Ru)₃O₄, trigonal Na₃Li(MoO₄)₂·6H₂O, ostensibly cubic Zr_{1-x-y}Ce_xGd_yO_{2-0.5y} and a lanthanoid (Nd,Gd,La,Ce) silicate. Zr_{1-x-y}Ce_xGd_yO_{2-0.5y} and lanthanoid (Nd,Gd,La,Ce) silicate were found exclusively in the Type II

microstructure as component crystal phases of ‘reprecipitated calcine’. Heat treated samples (simulating the retarded cooling experienced by actual (active) borosilicate HLW glasses after pouring) displayed extensive crystallisation and cracking (Type A microstructure) and/or ‘banded’ crystallisation (Type B microstructure) depending on their parent (as-cast) microstructure (Type I and/or Type II respectively). Crystal phases identified in heat treated samples were: tetragonal SiO_2 (α -cristobalite), tetragonal $(\text{Na,Sr,Nd,La})\text{MoO}_4$, cubic $\text{Ce}_{1-x-y}\text{Zr}_x\text{Gd}_y\text{O}_{2-0.5y}$, a Ni-rich phase, a lanthanoid (Nd,Gd,La,Ce) silicate and orthorhombic $\text{LiNaZrSi}_6\text{O}_{15}$ (zektzerite). α -cristobalite was found exclusively in the Type A microstructure, while lanthanoid (Nd,Gd,La,Ce) silicate and zektzerite were only found in the Type B microstructure. Potential host phases for HLW radionuclides are: Pd–Te alloy (^{107}Pd and ^{79}Se), $(\text{Cr,Fe,Ni,Ru})_3\text{O}_4$ (^{63}Ni), $\text{Zr}_{1-x-y}\text{Ce}_x\text{Gd}_y\text{O}_{2-0.5y}$ (^{93}Zr , Pu and U), both lanthanoid (Nd,Gd,La,Ce) silicates (Am and Cm), $(\text{Na,Sr,Nd,La})\text{MoO}_4$ (^{90}Sr , Am and Cm), $\text{Ce}_{1-x-y}\text{Zr}_x\text{Gd}_y\text{O}_{2-0.5y}$ (^{93}Zr , Pu and U), the Ni-rich phase (^{63}Ni) and zektzerite (^{93}Zr , ^{126}Sn and U). Cracking in samples was attributed to thermal expansion mismatch between the borosilicate HLW glass matrix and RuO_2 , cristobalite (both α and β), $(\text{Na,Sr,Nd,La})\text{MoO}_4$ and zektzerite on cooling. There was also a contribution from the cristobalite α – β phase transition.

PACS: 64.70.dg; 81.05.Kf; 28.41.Kw; 81.40.Gh; 81.05.Pj

1. Introduction

In the UK, spent nuclear fuel is reprocessed to recover Pu and U with the remaining solution being regarded as waste. The liquid waste arising from

reprocessing is termed high-level waste (HLW) due to the level of radioactivity and heat it generates. Liquid HLW is currently immobilised by vitrification in a mixed alkali borosilicate glass matrix. This provides a material suitable for storage and eventual disposal, envisioned to be in an underground repository located within a stable geological formation [1–7].

During vitrification some HLW components have limited solubility in the borosilicate glass melt, typically platinoids (Ru, Pd and Rh), high oxidation state cations (*e.g.* Mo⁶⁺, S⁶⁺ and Cr⁶⁺) and refractory oxides (*e.g.* Al₂O₃ and Cr₂O₃). These components of limited solubility can form crystal phases and/or an immiscible liquid (generally termed ‘yellow phase’) during glass melting [1–7]. Due to the radiogenic heat produced by decaying radionuclides the glass will experience retarded cooling from its melting temperature [1,3]. This retarded cooling can lead to further crystal phases precipitating in the glass (as can multiple glass pours into the same storage/disposal canister [8]), often nucleated and grown upon crystal phases formed during glass melting [7]. If immiscible ‘yellow phase’ forms during glass melting and persists until glass pouring it will crystallise on cooling [7].

Borosilicate HLW glasses incorporating crystal phases and/or ‘yellow phase’ can be described as glass composite materials (GCMs) as they are neither fully amorphous nor fully crystalline, although they are predominantly amorphous. Describing them as glass-ceramics would be incorrect as they are not crystallised by a controlled heat treatment to produce a desired microstructure and crystal phase(s). The component elements of GCMs can be chemically incorporated into the glass structure and/or physically encapsulated by the glass matrix (if incorporated into crystal phases and/or ‘yellow phase’). The product of immobilising waste in a suitable matrix is a wasteform [5,6].

The crystallisation (devitrification) of borosilicate HLW glasses and melts can have a variety of consequences. HLW radionuclides can partition into crystal phases and/or the glass matrix, depending on the crystal phase(s) formed [7]. The aqueous durability of crystal phases reported in borosilicate HLW glasses varies from high (such as spinels [9,10] and powellite-structured molybdates [7,11–13]) to low (for example the water-soluble portion of ‘yellow phase’ [3,12–23]). The effect of crystallisation on the aqueous durability of a wastefrom can range from beneficial [1,17] to detrimental [3,24–27], being a cumulative effect if multiple crystal phases are present. During glass melting molten ‘yellow phase’ can corrode glass melter [14,20,22,23,28–34] and increase the volatilisation of some component species [23,35–37]. Crystal phases in glass melts can sediment to the melter floor [2,20,25,38–42], forming a ‘sludge’ layer of higher density, electrical conductivity and viscosity, which can cause pouring difficulties [20,38–43] and short circuit submerged electrodes (if present) [2,38–41,44–46]. The thermal expansion coefficients (TECs) of crystal phases may differ from those of the surrounding glass matrix, which can generate stress and may eventually lead to cracking of the wastefrom on cooling [7]. Crystal phase formation may alter the TEC of the surrounding glass matrix by modifying its chemical composition [7]. Cracking of the glass matrix and/or crystal phases can also occur if the crystal phases undergo phase transitions on cooling [7]. Preferential aqueous corrosion at glass–crystal interfaces may occur [7,10,47–50] due to chemical composition gradients and/or stress caused by TEC mismatch and/or crystal phase transitions [48–50]. This is particularly undesirable since HLW radionuclides tend to concentrate at these interfaces [10,47]. Crystal phases present in actual (active) borosilicate HLW glasses may become metamict (amorphous) due to irradiation, thereby increasing in volume which can

generate stress and may eventually lead to cracking [3,51–53]. Cracking of a wastefrom can reduce its aqueous durability because its surface area increases [44]. Crystal phases incorporating HLW radionuclides may be detrimentally affected by nuclear transmutations (*e.g.* ^{90}Sr to ^{90}Y to ^{90}Zr) [7]. Ideally, crystal phases formed in borosilicate HLW glasses would have excellent aqueous durabilities, preferentially incorporate HLW radionuclides and be homogeneously distributed within a glass matrix of higher aqueous durability than the parent glass (due to the crystal phases preferentially incorporating elements detrimental to the aqueous durability of the glass matrix). In addition, the crystal phases would be radiation tolerant, nuclear transmutation tolerant, not undergo phase transitions on cooling and have TECs equal to, or larger than, the surrounding glass matrix [7].

This paper reports studies conducted on a simulated borosilicate HLW glass produced during inactive commissioning of a full-scale vitrification line at Sellafield, Cumbria, UK. This research aimed to identify the crystal phases present in as-cast samples, as well as determining which radionuclides may preferentially partition to them in actual borosilicate HLW glasses. It also aimed to identify the crystal phases formed after heat treating as-cast samples (simulating the retarded cooling experienced by radiogenically heated HLW glasses after pouring) and to determine which radionuclides may preferentially partition to these crystal phases in actual borosilicate HLW glasses.

2. Experimental

The simulated borosilicate HLW glass used in this work was supplied by Nexia Solutions Ltd and is termed Oxide glass. This trial composition simulates

vitrified oxide fuel (UO₂) reprocessing waste and was produced during inactive commissioning of a full-scale vitrification line at Sellafield, Cumbria, UK. The vitrification process at Sellafield is described elsewhere [1,2,7]. Received as-cast samples were from multiple pours and had not been annealed.

Heat treatment of as-cast samples was conducted in a temperature calibrated Lenton 1500 W muffle furnace with an air atmosphere. Samples of approximately 2 cm³ were cut from as-cast samples using a Struers Accutom-5 diamond saw and then placed on a bed of calcined alumina in a mullite tray. These were then held at 690 °C for 70 h before a 1 h anneal at 500 °C with heating and cooling rates of 5 °C min⁻¹. Any calcined alumina adhering to heat treated samples was removed.

Chemical analysis of Oxide glass samples was accomplished by combined X-ray fluorescence spectrometry (XRF) and direct current plasma atomic emission spectrometry (DCP-AES). An ARL 9400 Sequential XRF analysed Oxide glass samples for all elements heavier than boron using a Cu-filtered Rh X-ray source, a gas flow proportional counter employing P-10 gas (90% argon, 10% methane), a scintillation counter and was operated with a helium atmosphere. Three different Oxide glass samples were crushed in a steel percussion mortar, ground with an agate pestle and mortar and then sieved to <75 µm before analysis. UniQuant version 4.44 software (a universal, standardless analytical program) calculated the normalised chemical composition of each sample once their respective DCP-AES data (for B₂O₃ and Li₂O) were entered.

An SMI III DCP-AES utilising argon plasma analysed Oxide glass samples to determine wt% values for B₂O₃ and Li₂O after calibration with a multielement solution standard. Each of the three different Oxide glass samples prepared for XRF (<75 µm powders) had a sample placed in a Teflon container for microwave-assisted

acid digestion with HF–HNO₃ solution in a CEM MSP 1000 microwave. Digested samples were analysed alongside a digested multicomponent borosilicate glass standard (National Institute of Standards and Technology (NIST) standard reference material 1412) to ensure accuracy of the compositional data. After the B₂O₃ and Li₂O data from each sample had been added to its respective XRF data in UniQuant the three normalised chemical compositions were calculated, with the mean chemical composition being reported.

Archimedes' principle was used to calculate the unannealed as-cast sample density in deionised water at 21 °C. Three different as-cast samples were tested with the mean density being reported.

For differential thermal analysis (DTA) a Perkin Elmer DTA 7 running Perkin Elmer PYRIS version 5.00.02 thermal analysis software was used to determine the glass transition temperature (T_g) of Oxide glass by onset. The as-cast glass was crushed in a steel percussion mortar and then ground with an agate pestle and mortar before sieving to <75 µm. Both the sample and alumina reference material were placed in identical alumina crucibles and heated to 1000 °C at 5 °C min⁻¹ in a static air atmosphere.

Viscosity measurements of Oxide glass at high temperature were undertaken using a heat-shielded Brookfield DV-II+ viscometer. Samples were brought to temperature in a Pt crucible with a hemispherical base before insertion of the spindle. Melts were then allowed to equilibrate at temperature before measurements were taken.

Powder X-ray diffraction (XRD) of as-cast and heat treated samples was performed on Philips PW1710 and Siemens D500 diffractometers, both employing Ni-filtered Cu K α (K-L_{2,3}) radiation and operating at 40 kV and 30 mA. Both

machines operated in reflection mode, scanning from 10° to 80° 2θ at $0.1^\circ \text{ min}^{-1}$ in 0.01° steps. Samples were crushed in a steel percussion mortar, ground with an agate pestle and mortar, and sieved to $<75 \mu\text{m}$ before being placed in aluminium sample holders for loading into the machines. XRD traces were peak-matched to crystal phases detailed in the International Centre for Diffraction Data (ICDD) database using STOE WinX^{POW} version 1.06 software, after first being converted for use in WinX^{POW} by Traces version 4.2 software followed by WinFit! version 1.12 software.

Scanning electron microscope (SEM) analysis of as-cast and heat treated samples was conducted with a JEOL JSM 6400 operating at an accelerating voltage of 20 kV and equipped with a Link Analytical ISIS energy dispersive X-ray spectroscopy (EDX) system with beryllium window. Secondary electron (SE) and backscattered electron (BE) images were collected from samples, along with EDX spectra. Samples were sectioned to approximately 1 cm^3 using a Struers Accutom-5 diamond saw before mounting them in cold-setting epoxy resin (Struers EpoFix) under vacuum. Mounted samples were then ground with sequentially finer grit SiC papers (from 120 to 1200) and water before polishing to a finish of $1 \mu\text{m}$ with diamond pastes. Polished samples were partially painted with Acheson electrodag 1415M silver paint and then carbon coated using an Edwards “Speedivac” model 12E6/1598 coating unit before analysis.

Transmission electron microscope (TEM) investigation of as-cast and heat treated samples employed a Philips EM 420T(D) fitted with a Link Analytical eXL EDX system (with ATW2) and an FEI Tecnai 20 equipped with an EDAX Genesis EDX system (with SUTW). The microscopes operated with accelerating voltages of 120 kV and 200 kV respectively and both employed double-tilt sample holders. Bright-field (BF) micrographs and selected-area electron diffraction patterns, as well

as EDX spectra, were collected from samples. Samples were sectioned to approximately 500 μm thickness using a Struers Accutom-5 diamond saw before being mounted on a Gatan 623 disk grinder using heat-sensitive resin. Both sides of samples were subsequently ground with sequentially finer grit SiC papers (from 120 to 1200) and water to a final section thickness of approximately 30 μm . Sections were then cleaned of resin using acetone before 3.05 mm diameter copper rings with a 1 mm diameter aperture were attached using Devcon 5-minute epoxy glue. A Gatan Dual Ion Mill (DuoMill) model 600 operating with an accelerating voltage of 6 kV at a combined gun current of 0.6 mA subsequently milled the samples at an incidence angle of 15° (2 h) followed by 10° (to perforation). Milled samples were then carbon coated using an Edwards “Speedivac” model 12E6/1598 coating unit before analysis. Obtained electron diffraction patterns were indexed using simulated electron diffraction patterns produced with CaRIne Crystallography version 3.1 software. The space group, lattice parameters and atomic coordinates of crystal phases were needed for their simulation in CaRIne and were obtained from the Inorganic Crystal Structure Database (ICSD).

3. Results and discussion

3.1. Chemical, physical and thermal analysis

The chemical composition of Oxide glass is presented in Table 1, from which its waste loading (WL) and molar mass (M) were calculated (Table 2). The measured density (ρ) of unannealed as-cast Oxide glass allowed its unannealed molar volume (V_m) to be calculated using $V_m = M/\rho$ (Table 2). The glass transition temperature (T_g)

of Oxide glass is also given in Table 2. Oxide glass melts displayed non-Newtonian viscosity behaviour.

Non-Newtonian viscosity behaviour in borosilicate HLW glass melts has been observed previously and is thought to be caused by the presence of platinoid phases [12,19,40,41,54].

3.2. Phase and microstructural analysis

3.2.1. As-cast samples

Some as-cast samples had compositionally homogeneous glass matrices (Fig. 1(a)) termed Type I microstructure. Other as-cast samples had compositionally inhomogeneous glass matrices (Figs. 1(b) and 2(a)) termed Type II microstructure. The Type II microstructure displayed compositional ‘banding’ and frequently contained ‘reprecipitated calcine’. Occasionally as-cast samples displayed both Type I and Type II microstructures. An EDX line scan (Fig. 2) revealed the bright ‘bands’ (indicating higher average atomic number in that region) in the Type II microstructure were enriched in Ce, Cs, Gd, Mo, Nd, Ni and Zr (simulated HLW components) while being depleted in Si, relative to the bulk glass composition.

Type I microstructure indicates the as-cast samples had sufficient reaction time between the base glass frit and the simulated HLW calcine in the glass melter before pouring to form a homogeneous glass. Type II microstructure indicates that the base glass frit and simulated HLW calcine had insufficient reaction time in the glass melter before pouring to form a homogeneous glass. Less than 1 h residence time in the glass melter is suggested by the presence of ‘reprecipitated calcine’ and bubbles [1,20,55], and also compositional ‘banding’ [20,56]. Wasteform aqueous durability

will be detrimentally affected by this compositional ‘banding’, the ‘bands’ enriched in simulated HLW components being of lower aqueous durability than the ‘bands’ enriched in base glass [56]. The internal microstructure of ‘reprecipitated calcine’ consisted of two crystal phases, $Zr_{1-x-y}Ce_xGd_yO_{2-0.5y}$ and lanthanoid (Nd,Gd,La,Ce) silicate, consistent with previous reports [20,55]. These crystal phases will have precipitated from the glass melt on cooling due to local supersaturation of their component elements [55]. ‘Reprecipitated calcine’ in a borosilicate HLW glass will be preferentially leached, lowering the overall aqueous durability of the wasteform [57].

3.2.1.1. RuO₂ RuO₂ (rutile crystal structure, tetragonal crystal system, space group $P4_2/mnm$) was identified in as-cast samples by XRD (labelled \blacklozenge in Fig. 3(a) and (b)) using ICDD card [40-1290]. RuO₂ crystals had acicular morphologies (Fig. 4(a)–(c)), while a globular Ru inclusion (Fig. 4(d)) was proposed to be Ru metal. A RuO₂ crystal contacting other RuO₂ crystals is shown in Fig. 4(b), while an uncommonly large RuO₂ crystal had cracks emanating from it perpendicular to the long axis of the crystal (arrowed in Fig. 4(c)). An EDX line scan (Fig. 2) revealed RuO₂ crystals/Ru metal inclusions were randomly distributed throughout the glass matrix of even a compositionally inhomogeneous as-cast sample (Type II microstructure). RuO₂ crystals were found in both Type I and Type II microstructures.

RuO₂ crystals are common in borosilicate HLW glasses [1,8,12,19,25,39–41,43,46,54,56,58–68], often having acicular morphologies [1,12,39,40,46,54,69,70] and incorporating Rh if present, forming (Ru,Rh)O₂ crystals [3,39–41,67,69–72]. Ru metal inclusions in borosilicate HLW glasses have been reported previously [41,66,73]. The RuO₂ crystal contacting neighbouring RuO₂ crystals was part of a

cluster which could have agglomerated into a larger cluster before sedimenting to the bottom of the glass melter [2,20,25,38–41]. The uncommonly large RuO₂ crystal would sediment more quickly in a glass melt due to its size [67]. A ‘sludge’ layer enriched in RuO₂ crystals at the bottom of a glass melter would be of higher electrical conductivity, density and viscosity than the bulk glass melt. This could cause pouring difficulties [20,38–43] and potentially short circuit submerged electrodes (if present) [2,38–41,44–46]. The uncommonly large RuO₂ crystal with cracks emanating from it perpendicular to the long axis of the crystal indicates the glass is in tension along this axis. Table 3, detailing TECs, offers an explanation for this behaviour where the long axis of the crystal is also the crystallographic *c*-axis which expands on cooling, putting the glass matrix in this direction into tension and leading to cracking. The thermal expansion behaviour of both RhO₂ and (Ru,Rh)O₂ are not known to the authors. RuO₂ crystals are known to form in actual borosilicate HLW glasses [71] (demonstrating their radiation tolerance) and can act as nuclei for further crystallisation during the radiogenically retarded cool of these glasses [43,58,60,62,69,75]. Sloping melter floors coupled with a bottom drain can reduce the retention of sedimented material (such as RuO₂ crystals) in glass melters [40,67] although this approach is not employed at Sellafield. The presence of platinoid phases (such as RuO₂ crystals) in borosilicate HLW glasses is reported to have a negligible [54], if not a positive effect on their aqueous durabilities [72].

3.2.1.2. Pd–Te alloy Pd–Te alloy (face-centred cubic (fcc) crystal structure, cubic crystal system, space group $Fm\bar{3}m$) was identified in as-cast samples by XRD (labelled ● in Fig. 3(b)) using the Pd metal ICDD card [46-1043]. Pd–Te alloy inclusions generally had spheroidal morphologies (Fig. 5(a)) but were sometimes

globular (Fig. 5(b)). Pd–Te alloy inclusions were found in both Type I and Type II microstructures.

Pd–Te alloy inclusions have been noted in other borosilicate HLW glasses [3,39,41,54,59,66,67,71], often with spheroidal morphologies [25,39,40]. Some, if not all, of the Pd–Te alloy inclusions had the fcc structure (according to XRD), indicating their Te content is ≤ 16 at% [76]. Because Pd and Rh form a complete solid solution above 910 °C [77] Pd–Te alloy inclusions can incorporate Rh if it is present in the borosilicate HLW glass, forming Pd–Rh–Te alloy inclusions [19,40,41,63,69,70,72]. The elements Te and Se have similar chemistries (both are from Group 16 in the Periodic Table) so Se could be incorporated into Pd–Te alloy inclusions, as has been observed previously in a borosilicate HLW glass [67]. The maximum content of Se in fcc Pd is 1.5 at% [78]. The authors do not know of a quaternary Pd–Rh–Se–Te phase diagram. Pd–Te alloy inclusions are an effective nucleating agent [3,69] and have been observed to form in actual borosilicate HLW glasses [71], demonstrating their radiation tolerance. A ‘sludge’ layer enriched in Pd–Te alloy inclusions at the bottom of a glass melter (due to sedimentation) would be of higher electrical conductivity, density and viscosity than the bulk glass melt. As already noted, this could cause pouring problems [20,38–43] and potentially short circuit submerged electrodes (if present) [2,38–41,44–46]. Sloping melter floors coupled with a bottom drain can reduce the retention of sedimented material (such as Pd–Te alloy inclusions) in glass melters [40,67] although this approach is not employed at Sellafield. The formation of Pd–Te alloy inclusions oxidises the glass melt [66]. As already noted, the presence of platinoid phases (such as Pd–Te alloy inclusions) in borosilicate HLW glasses have been reported to have a negligible [54], if not a positive effect on their aqueous durabilities [72]. Pd–Te alloy inclusions are a potential host for ^{107}Pd and ^{79}Se .

3.2.1.3. $(Cr,Fe,Ni,Ru)_3O_4$ $(Cr,Fe,Ni,Ru)_3O_4$ (spinel crystal structure, cubic crystal system, space group $Fd\bar{3}m$) was identified in as-cast samples by XRD (labelled \diamond in Fig. 3(a)) using the $CuGa_2O_4$ ICDD card [44-183]. $CuGa_2O_4$ was not present in as-cast samples (as can be seen from the chemical composition in Table 1), instead a spinel-structured crystal phase with matching lattice parameters but different chemical composition was present, in this case $(Cr,Fe,Ni,Ru)_3O_4$ (by qualitative EDX). $(Cr,Fe,Ni,Ru)_3O_4$ crystals had faceted morphologies (Fig. 6(a) and (b)). The spinel crystal structure of $(Cr,Fe,Ni,Ru)_3O_4$ was confirmed by electron diffraction using the data of Della Giusta *et al.* [79]. A cluster of faceted $(Cr,Fe,Ni,Ru)_3O_4$ crystals is shown in Fig. 6(b). $(Cr,Fe,Ni,Ru)_3O_4$ crystals were found in both Type I and Type II microstructures.

Spinel crystals of similar composition to $(Cr,Fe,Ni,Ru)_3O_4$ have been reported in other borosilicate HLW glasses [32,43,62,75]. Natural spinels can incorporate Ru like the $(Cr,Fe,Ni,Ru)_3O_4$ crystals do [80] and as natural spinels can also incorporate Rh [80] it is anticipated that spinel crystals precipitated in borosilicate HLW glasses containing Rh will do also. The formation of $(Cr,Fe,Ni,Ru)_3O_4$ crystals would have negligible impact on wastefrom aqueous durability [3,81] probably because they do not incorporate glass network formers. The observed $(Cr,Fe,Ni,Ru)_3O_4$ crystal cluster could sediment quickly in a borosilicate HLW glass melt due to its size [67], likely contributing to a 'sludge' layer at the bottom of the glass melter [2,25,42] which could cause pouring difficulties [20,38,39,41–43]. Spinel crystals are known to nucleate and grow on platinoid phases [43,58,62,67,73], and in turn can act as nucleation sites for other crystal phases [62,73]. Spinel crystals in borosilicate HLW glasses have higher aqueous durabilities than the surrounding glass matrix [9,10] and are radiation tolerant

[82], as evidenced by their formation in actual borosilicate HLW glasses [71,81].
(Cr,Fe,Ni,Ru)₃O₄ crystals are a potential host for ⁶³Ni (an activation product).

3.2.1.4. *Na₃Li(MoO₄)₂·6H₂O* Na₃Li(MoO₄)₂·6H₂O (trigonal crystal system, space group $R\bar{3}c$) was identified in as-cast samples by XRD (labelled □ in Fig. 3(b)) using ICDD card [30-769]. Na₃Li(MoO₄)₂·6H₂O was not observed in as-cast samples by microscopy, probably due to the use of water in sample preparation (in which it will dissolve).

Na₃Li(MoO₄)₂·6H₂O will have formed through the hydration of its parent alkali molybdate phase by atmospheric H₂O. Na₃Li(MoO₄)₂·6H₂O is water-soluble [12] and has been identified in ‘yellow phase’ [7,12]. Immiscible ‘yellow phase’ can form during borosilicate HLW glass melting, the molten ‘yellow phase’ segregating from the glass melt during feed-to-glass conversion [20,23,28,29,34]. Molten ‘yellow phase’ is generally found on the surface of the glass melt [2,13,14,18,20,21,29,31,34–36,40,44,64,83] where it is highly corrosive to melter linings (both metal and ceramic) [14,20,22,23,28–34] and can increase the volatilisation of some component species [23,35–37]. The radionuclides ¹³⁷Cs, ⁹⁰Sr, ³⁶Cl, ¹³⁵Cs and ⁹⁹Tc preferentially partition to molten ‘yellow phase’ [5–7,12–18,20,21,23,31,32,35,36,84]. In the solid state ‘yellow phase’ is an assembly of crystal phases whose number, structures and chemical compositions will depend on the borosilicate HLW glass feed composition [3,13,20–22,30], with the component crystal phases being predominantly water-soluble [3,12–23]. ‘Yellow phase’ gets its name from its colour in the solid state, thought to be caused by the presence of chromates [3,17,83].

3.2.1.5. $Zr_{1-x-y}Ce_xGd_yO_{2-0.5y}$ Globular agglomerates of $Zr_{1-x-y}Ce_xGd_yO_{2-0.5y}$ nanocrystals (Fig. 7(a)) were identified by their dark speckled contrast features (when viewed by TEM), approximately 3–17 nm in size (Fig. 7(b)). The ring electron diffraction pattern obtained from this phase (Fig. 7(c)) confirmed the nanocrystals are randomly oriented. Electron diffraction (Fig. 7(c)) indicated $Zr_{1-x-y}Ce_xGd_yO_{2-0.5y}$ had the fluorite crystal structure (space group $Fm\bar{3}m$) using the data of Bouvier *et al.* [85]. Globular agglomerates of $Zr_{1-x-y}Ce_xGd_yO_{2-0.5y}$ nanocrystals were associated with bubbles (Fig. 7(a)), larger lanthanoid (Nd,Gd,La,Ce) silicate crystals with hexagonal morphology (Fig. 8) and by extension were a component crystal phase of ‘reprecipitated calcine’ (Fig. 1(b)). $Zr_{1-x-y}Ce_xGd_yO_{2-0.5y}$ nanocrystals were not associated with unidentified XRD peaks in Fig. 3(a) and were found exclusively in the Type II microstructure.

An ostensibly cubic ZrO_2 crystal phase (incorporating Ce and Sm), similar to $Zr_{1-x-y}Ce_xGd_yO_{2-0.5y}$, has previously been reported in a borosilicate HLW glass [86]. The incorporation of Ce and Gd in $Zr_{1-x-y}Ce_xGd_yO_{2-0.5y}$ nanocrystals helps to stabilise them in cubic form [87] because of their larger ionic radii. Due to their structural similarity to CeO_2 (fluorite crystal structure), $Zr_{1-x-y}Ce_xGd_yO_{2-0.5y}$ nanocrystals could potentially incorporate Pu [3,84,88] and U [72,89] were they to form in actual borosilicate HLW glasses. $Zr_{1-x-y}Ce_xGd_yO_{2-0.5y}$ nanocrystals are also a potential host for ^{93}Zr . The agglomerates of $Zr_{1-x-y}Ce_xGd_yO_{2-0.5y}$ nanocrystals likely formed by precipitation upon cooling a glass melt locally supersaturated in their component elements [55], forming a component crystal phase of ‘reprecipitated calcine’ [20,55]. This would also explain the regular size of the nanocrystals (approximately 3–17 nm), indicative of precipitation upon cooling due to supersaturation [90]. As $Zr_{1-x-y}Ce_xGd_yO_{2-0.5y}$ nanocrystals are expected to be radiation tolerant [82] they may

form in actual borosilicate HLW glasses. A problem for agglomerates of $Zr_{1-x-y}Ce_xGd_yO_{2-0.5y}$ nanocrystals may be preferential corrosion between the nanocrystals during aqueous leaching [10].

The crystal structure of ZrO_2 doped with CeO_2 and Gd_2O_3 (analogous to the $Zr_{1-x-y}Ce_xGd_yO_{2-0.5y}$ nanocrystals) can vary from tetragonal (t, space group $P4_2/nmc$) to cubic (c, space group $Fm\bar{3}m$) with decreasing levels of ZrO_2 . Between these two forms lie metastable t' (space group $P4_2/nmc$, axial ratio $c/a > 1$) and then pseudocubic t'' (an intermediate form between t' and c, space group $P4_2/nmc$, axial ratio $c/a = 1$) [87]. XRD and electron diffraction are usually not sensitive enough to the oxygen displacements associated with these different forms to differentiate between them (especially with the peak broadening associated with nanocrystalline phases) so Raman spectroscopy is generally used [87,91]. Unfortunately the $Zr_{1-x-y}Ce_xGd_yO_{2-0.5y}$ nanocrystals contain Gd^{3+} cations so oxygen vacancies in the crystals will reduce the effectiveness of Raman spectroscopy [87]. Therefore, while we have no direct evidence, the $Zr_{1-x-y}Ce_xGd_yO_{2-0.5y}$ nanocrystals are expected to be cubic (c) or pseudocubic (t'') as nanocrystals of this size (≤ 17 nm) help stabilise CeO_2 -doped ZrO_2 as t''/c [91].

3.2.1.6. Lanthanoid (Nd,Gd,La,Ce) silicate Lanthanoid (Nd,Gd,La,Ce) silicate crystals with hexagonal morphologies were observed in as-cast samples (Fig. 8), their chemical composition was determined qualitatively by EDX. B, Li and Na may also have been present but could not be detected by EDX in our SEM. This crystal phase was not detected in as-cast samples by XRD or TEM so its crystal structure is unidentified. Hexagonal lanthanoid (Nd,Gd,La,Ce) silicate crystals were associated with bubbles, globular agglomerates of $Zr_{1-x-y}Ce_xGd_yO_{2-0.5y}$ nanocrystals and cracking

(Fig. 8), and by extension were a component crystal phase of ‘reprecipitated calcine’ (Fig. 1(b)). Lanthanoid (Nd,Gd,La,Ce) silicate crystals were likely associated with unidentified XRD peaks in Fig. 3(a) and were found exclusively in the Type II microstructure.

Lanthanoid (Nd,Gd,La,Ce) silicate crystals likely formed by precipitation upon cooling a glass melt locally supersaturated in their component elements [55], forming a component crystal phase of ‘reprecipitated calcine’ [20,55]. As lanthanoid (Nd,Gd,La,Ce) silicate crystals were associated with cracking their thermal expansion behaviour is probably different from that of the surrounding glass matrix.

Furthermore, lanthanoid (Nd,Gd,La,Ce) silicate crystals are a potential host for Am and Cm as both are present in the +3 oxidation state in borosilicate HLW glasses [51] and have similar ionic radii to Nd [92].

3.2.2. Heat treated samples

Some heat treated samples displayed extensive crystallisation (Fig. 9(a) and (b)) and cracking (Fig. 9(c)). This microstructure was Type I (Fig. 1(a)) before heat treatment so is termed Type A microstructure. Other heat treated samples displayed ‘banded’ crystallisation (Fig. 9(d)) and phases not observed in Type A microstructure. This second microstructure was the result of heat treating a Type II microstructure (Fig. 1(b)) so is termed Type B microstructure. Fig. 10(a) is a typical XRD trace from heat treated samples with Type A microstructure. Fig. 10(b) is a typical XRD trace from heat treated samples with Type B microstructure. RuO₂ crystals (labelled ♦ in Fig. 10(a) and (b)) and Pd–Te alloy inclusions (labelled ● in Fig. 10(a)) were already present in the as-cast samples (Fig. 3). Occasionally heat treated samples displayed both Type A and Type B microstructures.

Cracking seen in the Type A microstructure may be detrimental to wastefrom aqueous durability due to the potential increase in its surface area [44]. The ‘bands’ of crystallisation displayed by the Type B microstructure formed from the ‘bands’ enriched in simulated HLW components in the parent (Type II) microstructure. Minimal cracking in the Type B microstructure indicates little thermal expansion mismatch between the glass matrix and encapsulated crystal phases. This negligible potential increase in wastefrom surface area is not expected to detrimentally affect wastefrom aqueous durability.

As a point of interest, acicular Ni- and Te-rich crystals of unidentified composition (such as alloy, oxide or telluride) were observed protruding from the surface of heat treated samples with Type B microstructure.

3.2.2.1. SiO₂ (α -cristobalite) SiO₂ (α -cristobalite, tetragonal crystal system, space group *P4₁2₁2*) was identified in heat treated samples by XRD (labelled \diamond in Fig. 10(a)) using ICDD card [39-1425]. α -cristobalite crystals generally had dendritic morphologies (Fig 11(a) and (b)) but were sometimes globular. Fig. 11(b) shows cracking in and around dendritic α -cristobalite crystals. α -cristobalite crystals were not observed in heat treated samples by TEM and were found exclusively in the Type A microstructure.

α -cristobalite is the major crystal phase seen in heat treated samples with the Type A microstructure and has been reported to form in other borosilicate glasses [15,53,63,65,69,89,93–96]. Dendritic and globular morphologies for α -cristobalite crystals in borosilicate HLW glasses have been reported [15]. Cristobalite is responsible for the extensive cracking seen in the Type A microstructure, a cumulative effect of the α - β phase transition which results in a decrease in crystal

volume on cooling [65,93] and also TEC mismatch (for both α - and β -cristobalite) with the surrounding glass matrix [95]. Table 3 shows that as the borosilicate HLW glass cools β -cristobalite contracts more slowly than the surrounding glass matrix putting the glass matrix in tension and causing its cracking. As the α - β phase transition region is passed there is a volume decrease in the cristobalite which will cause internal cracking as the crystal is physically anchored to the surrounding glass matrix by its dendritic morphology. This internal cracking and voiding will continue as the crystal cools to room temperature due to the faster contraction of α -cristobalite compared to the surrounding glass matrix. The formation of cristobalite crystals would be detrimental to wasteform aqueous durability as their precipitation removes SiO_2 from the surrounding glass matrix [7,49,63,69,93,96], resulting in a glass of lower aqueous durability than the parent glass, especially around the crystals [69]. Glass matrix cracking around α -cristobalite crystals may increase wasteform surface area, which could lower overall aqueous durability [44]. α -cristobalite crystals may not be encountered in actual borosilicate HLW glasses as they are electron beam sensitive [100] and therefore would not form in an environment with excessive β and γ radiation [101], let alone α radiation. This explains why no α -cristobalite crystals were observed by TEM. However, as the amorphous phase separation (APS) of a borosilicate HLW glass has been observed prior to cristobalite crystallisation [65] and APS of alkali borosilicate glasses is enhanced by electron irradiation [101], the formation of a vitreous silica phase would have much the same effect on wasteform aqueous durability as cristobalite formation [50,94]. As Al_2O_3 additions can inhibit cristobalite crystallisation in alkali borosilicate glasses [95] and there is little Al_2O_3 in Oxide glass it is suggested that increasing the amount of Al_2O_3 in Oxide glass may inhibit cristobalite formation. Al_2O_3 additions to Oxide glass would also be beneficial

as they have been shown to suppress APS in sodium borosilicate glasses [50] and can also improve the aqueous durability of borosilicate HLW glasses [2,3,102–104].

3.2.2.2. $(Na,Sr,Nd,La)MoO_4$ $(Na,Sr,Nd,La)MoO_4$ (powellite crystal structure, tetragonal crystal system, space group $I4_1/a$) was identified in heat treated samples by XRD (labelled \square in Fig. 10(a)) using the $NaLa(MoO_4)_2$ and $AgLaMo_2O_8$ ICDD cards [24-1103] and [49-384]. $NaLa(MoO_4)_2$ or $AgLaMo_2O_8$ were not present in glass samples, instead a powellite-structured crystal phase with matching lattice parameters but different chemical composition was present, in this case $(Na,Sr,Nd,La)MoO_4$ (by qualitative EDX). Li may also have been present but could not be detected by EDX. $(Na,Sr,Nd,La)MoO_4$ crystals had dendritic morphologies (Fig. 12). The powellite crystal structure of $(Na,Sr,Nd,La)MoO_4$ was confirmed by electron diffraction using the data of Hazen *et al.* [105]. Dendritic $(Na,Sr,Nd,La)MoO_4$ crystals were noted to nucleate and grow on RuO_2 crystals (Fig. 12) as well as Pd–Te alloy inclusions. Fig. 12 also shows a dendritic $(Na,Sr,Nd,La)MoO_4$ crystal with internal cracking (arrowed) perpendicular to its long axis. $(Na,Sr,Nd,La)MoO_4$ crystals were found in both Type A and Type B microstructures.

Powellite-structured molybdates of similar composition to $(Na,Sr,Nd,La)MoO_4$ have previously been reported in borosilicate HLW glasses [22,25,33,61,64,68,69,89], some with its dendritic morphology [15,22,25,33]. Powellite-structured molybdates have also been noted to nucleate and grow on platinoid phases (RuO_2 crystals and Pd–Te alloy inclusions) [25]. Table 3 offers an explanation for the cracking in the $(Na,Sr,Nd,La)MoO_4$ crystal perpendicular to its long axis. The crystallographic *c*-axis of powellite contracts on cooling at more than twice the rate of the borosilicate HLW glass matrix and as the crystal is physically

anchored to the glass matrix by its dendritic morphology this will lead to tension along the *c*-axis, eventually causing cracking in the crystal perpendicular to this tension, indicating that the long axis of the crystal is also the crystallographic *c*-axis. Powellite-structured molybdates have been reported to form in actual borosilicate HLW glasses [71], demonstrating their radiation tolerance. Powellite-structured molybdates are water-insoluble [7,11–13], their crystallisation reducing the leach rate of elements incorporated by them [26] and slightly improving the overall wastefrom aqueous durability [54]. (Na,Sr,Nd,La)MoO₄ crystals are a potential host for ⁹⁰Sr, as well as for Am and Cm [107] as both are in the +3 oxidation state in borosilicate HLW glasses [51] and have similar ionic radii to Nd [92]. Powellite-structured molybdates have been reported to form in the altered surface layers of borosilicate HLW glasses during high temperature and/or long-term aqueous durability tests [107–109].

3.2.2.3. $Ce_{1-x-y}Zr_xGd_yO_{2-0.5y}$ $Ce_{1-x-y}Zr_xGd_yO_{2-0.5y}$ (fluorite crystal structure, cubic crystal system, space group $Fm\bar{3}m$) was identified in heat treated samples by XRD (labelled ■ in Fig. 10(b)) using the CeO₂ ICDD card [34-394]. $Ce_{1-x-y}Zr_xGd_yO_{2-0.5y}$ crystals had spheroidal morphologies and displayed crystal twinning (Fig. 13(a)). The fluorite crystal structure of $Ce_{1-x-y}Zr_xGd_yO_{2-0.5y}$ was confirmed by electron diffraction using the data of Taylor [110]. Occasionally Ru was noted in EDX spectra from $Ce_{1-x-y}Zr_xGd_yO_{2-0.5y}$ crystals. Compositional zoning of a spheroidal $Ce_{1-x-y}Zr_xGd_yO_{2-0.5y}$ crystal was observed in Fig. 15 (at the start (left) of the EDX line scan) where the core of the crystal was more enriched in Zr than the exterior and the exterior more enriched in Ce than the core. $Ce_{1-x-y}Zr_xGd_yO_{2-0.5y}$ crystals were predominantly found in the Type B microstructure.

$Ce_{1-x-y}Zr_xGd_yO_{2-0.5y}$ crystals are similar to crystal phases previously reported in borosilicate HLW glasses [3,17,19,25,54,58,64,68,69,72,89]. The Ru occasionally noted in EDX spectra from $Ce_{1-x-y}Zr_xGd_yO_{2-0.5y}$ crystals is due to RuO_2 crystals either nucleating the $Ce_{1-x-y}Zr_xGd_yO_{2-0.5y}$ and/or being enveloped by it as it grew, as has been observed before [54]. The compositional zoning observed in a $Ce_{1-x-y}Zr_xGd_yO_{2-0.5y}$ crystal is similar to that previously noted for a crystal phase in a borosilicate HLW glass [111] and could indicate that the $Ce_{1-x-y}Zr_xGd_yO_{2-0.5y}$ crystal exhibiting zoning grew from a globular agglomerate of $Zr_{1-x-y}Ce_xGd_yO_{2-0.5y}$ nanocrystals. $Ce_{1-x-y}Zr_xGd_yO_{2-0.5y}$ crystals are anticipated to be radiation tolerant [82], demonstrated by similar crystal phases forming in actual borosilicate HLW glasses [71]. $Ce_{1-x-y}Zr_xGd_yO_{2-0.5y}$ crystals are a potential host for Pu [3,84,88] and U [72,89], and are anticipated to be chemically durable [7,107].

3.2.2.4. Ni-rich phase Ni-rich crystals with acicular morphologies (Fig. 13(b)) were a nickel oxide phase containing some Cr and Fe (by qualitative EDX). Clusters of acicular Ni-rich crystals (Figs. 13(b) and 15(a)) nucleated and grew on RuO_2 crystals and Pd–Te alloy inclusions. Electron diffraction of this Ni-rich phase revealed it was crystalline although its crystal structure could not be identified. These Ni-rich crystals were likely associated with unidentified XRD peaks in Fig. 10(a) and (b), and were predominantly found in the Type B microstructure.

Although the crystal structure for the Ni-rich phase could not be determined, it is possible it is bunsenite (NiO) with substitution of some Cr and Fe on the Ni-site, and Ni-site vacancies if the Cr and Fe are not all in the +2 oxidation state. Bunsenite has previously been reported in a borosilicate HLW glass [112]. This Ni-rich crystal phase is morphologically and compositionally similar to a Ni-rich phase of

unidentified crystal structure observed by Mitamura *et al.* [69]. As these Ni-rich crystals are electron beam stable in the TEM they may form in actual borosilicate HLW glasses [101]. The Ni-rich crystals are a potential host for ^{63}Ni (an activation product).

3.2.2.5. *Lanthanoid (Nd,Gd,La,Ce) silicate* Lanthanoid (Nd,Gd,La,Ce) silicate crystals with acicular/platy morphologies were observed in heat treated samples (Fig. 14(a)), their chemical composition was determined by qualitative EDX. B and Li may also have been present but could not be detected by EDX in our TEMs. Electron diffraction of this phase revealed it was crystalline although its crystal structure could not be identified. Fig. 15 (at the end (right) of the EDX line scan) revealed lanthanoid (Nd,Gd,La,Ce) silicate crystals had a lower Si concentration than the surrounding glass matrix. Lanthanoid (Nd,Gd,La,Ce) silicate crystals were likely associated with unidentified XRD peaks in Fig. 10(b) and were found exclusively in the Type B microstructure.

The crystal structure of lanthanoid (Nd,Gd,La,Ce) silicate was not identified by XRD or TEM (electron diffraction) as either of the two most likely candidates (due to their chemical composition and presence in other borosilicate HLW glasses): silicate apatite [3,19,24,51,53,61,68] or stillwellite [3,59,69]. The lack of cracking in or around lanthanoid (Nd,Gd,La,Ce) silicate crystals suggests it has TECs comparable to the surrounding glass matrix and therefore has a different crystal structure to the as-cast lanthanoid (Nd,Gd,La,Ce) silicate (which was associated with cracking, possibly due to TEC mismatch with the surrounding glass matrix). As lanthanoid (Nd,Gd,La,Ce) silicate crystals had a lower concentration of Si than the surrounding glass matrix their formation should have a beneficial effect upon the aqueous

durability of the surrounding glass and hence wastefrom. The stability of lanthanoid (Nd,Gd,La,Ce) silicate crystals under the electron beam suggests they may form in actual borosilicate HLW glasses [101]. Lanthanoid (Nd,Gd,La,Ce) silicate crystals are a potential host for Am and Cm as both are present in the +3 oxidation state in borosilicate glass [51] and have similar ionic radii to Nd [92]. Considering these positives, if this phase also has a high aqueous durability then it has the potential to be the basis of a glass-ceramic wastefrom for Am and Cm.

3.2.2.6. $LiNaZrSi_6O_{15}$ (zektzerite) $LiNaZrSi_6O_{15}$ (zektzerite, orthorhombic crystal system, space group *Cmca*) was identified in heat treated samples by XRD (labelled ○ in Fig. 10(b)) using ICDD card [29-835]. Zektzerite crystals had acicular morphologies (Figs. 14(b) and 15(a)). An EDX line scan (Fig. 15) revealed zektzerite crystals had a higher concentration of Si and Zr than the surrounding glass matrix. Zektzerite crystals had cracks emanating from them perpendicular to the long axis of the crystals and also displayed internal cracking (Figs. 14(b) and 15(a)). Fig. 14(b) shows acicular zektzerite crystals penetrating lanthanoid (Nd,Gd,La,Ce) silicate crystals. Zektzerite crystals were not observed in heat treated glass samples by TEM and were found exclusively in the Type B microstructure.

Zektzerite crystals have previously been noted in a borosilicate HLW glass [59]. Zektzerite crystals are enriched in ZrO_2 (theoretically 23.26 wt%/12.5 mol%) and SiO_2 (theoretically 68.06 wt%/75 mol%) compared to the glass matrix. As zektzerite crystals require six of the eight moles for their formation to be SiO_2 their crystallisation in a borosilicate HLW glass will likely be detrimental to the aqueous durability of the surrounding glass matrix and hence wastefrom. The thermal expansion behaviour of zektzerite crystals detailed in Table 3 appears inconsistent

with the cracking observed in heat treated samples, where cracks are perpendicular to the long axis of the acicular crystals. This indicates that the crystallographic axis associated with the long axis of the crystal has a smaller or even negative thermal expansion coefficient compared to the other axes. The data of Shaikh [114] agree with observed cracking by indicating that the crystallographic *c*-axis has a negative TEC, meaning the crystal will expand along this axis on cooling thereby putting the glass matrix in this direction into tension while the crystal itself is in compression along this axis. This would cause stress and eventual cracking in the glass matrix perpendicular to the crystallographic *c*-axis, indicating that the long axis of the crystal is also the crystallographic *c*-axis. Glass matrix cracking around zektzerite crystals may increase wastefrom surface area, which could lower the overall aqueous durability of the wastefrom [44]. As zektzerite crystals often penetrated lanthanoid (Nd,Gd,La,Ce) silicate crystals it is concluded that they crystallised first.

Zektzerite crystals are a potential host for ^{93}Zr and U [109]. Zektzerite crystals are also a potential host for ^{126}Sn because Sn is predominantly in the +4 oxidation state and coordinated to six oxygens in borosilicate HLW glasses [115] (as is Zr in borosilicate HLW glasses and zektzerite [116]) and has a similar ionic radius to Zr^{4+} [92], demonstrated by $\text{LiNaSnSi}_6\text{O}_{15}$ being isostructural with zektzerite [113]. Zektzerite crystals have been reported to form in the altered surface layers of a borosilicate HLW glass during high temperature aqueous durability testing [109].

4. Conclusions

Insufficient reaction time in the glass melter between simulated HLW calcine and base glass frit resulted in as-cast samples with inhomogeneous microstructures.

The observed variability in microstructural homogeneity of as-cast samples indicates inconsistent process control during inactive commissioning of the full-scale vitrification line. This is to be expected as the trial vitrification runs were used to determine optimum processing conditions. The differing devitrification behaviour (in terms of microstructure and crystal phase composition) of as-cast samples upon heat treatment (to simulate the retarded cooling experienced by radiogenically heated HLW glasses after pouring) was a direct result of their as-cast microstructural homogeneity, despite samples having identical chemical compositions. This illustrates the importance of consistently maintaining optimal process control during HLW vitrification.

The potential incorporation of HLW radionuclides into identified crystal phases has been determined: Pd–Te alloy (^{107}Pd and ^{79}Se), $(\text{Cr,Fe,Ni,Ru})_3\text{O}_4$ (^{63}Ni), $\text{Zr}_{1-x-y}\text{Ce}_x\text{Gd}_y\text{O}_{2-0.5y}$ (^{93}Zr , Pu and U), both lanthanoid (Nd,Gd,La,Ce) silicates (Am and Cm), $(\text{Na,Sr,Nd,La})\text{MoO}_4$ (^{90}Sr , Am and Cm), $\text{Ce}_{1-x-y}\text{Zr}_x\text{Gd}_y\text{O}_{2-0.5y}$ (^{93}Zr , Pu and U), the Ni-rich phase (^{63}Ni) and zektzerite (^{93}Zr , ^{126}Sn and U). Preferential partitioning of SiO_2 into cristobalite and zektzerite has also been identified. The platinoid phases (RuO_2 and Pd–Te alloy) acted as nucleation sites for further crystallisation on heat treatment of as-cast samples. The potential effect of crystallisation on wasteform aqueous durability has been assessed, with a water-soluble crystal phase $(\text{Na}_3\text{Li}(\text{MoO}_4)_2 \cdot 6\text{H}_2\text{O})$ and crystal phases which decrease the aqueous durability of the surrounding glass matrix (cristobalite and zektzerite) being identified. Cracking in as-cast and heat treated glass samples was attributed to thermal expansion mismatch between certain crystal phases (RuO_2 , cristobalite (both α and β), $(\text{Na,Sr,Nd,La})\text{MoO}_4$ and zektzerite) and the surrounding glass matrix, as well as the cristobalite α – β phase transition, on cooling.

Increasing the quantity of Al₂O₃ in Oxide glass may increase the aqueous durability of this wasteform and prevent the amorphous phase separation of its glass matrix and the crystallisation of cristobalite. The lanthanoid (Nd,Gd,La,Ce) silicate formed in heat treated samples is a potential host phase for Am and Cm, and is worthy of further investigation.

Acknowledgements

The authors are indebted to Prof. Ian L. Pegg for granting P.B.R. a research visit to the Vitreous State Laboratory (VSL), The Catholic University of America, Washington, DC, USA. P.B.R. is also extremely grateful to the staff and students of the VSL for all their help and generosity during his visit. For funding this visit we thank the Sheffield Metallurgical and Engineering Association, the Laverick–Webster–Hewitt Travelling Fellowship, the Tom Jackson Travel Fund and the Armourers & Brasiers' Gauntlet Trust in conjunction with British Alcan Aluminium. The EPSRC (Industrial CASE studentship award number 01300676), Nexia Solutions Ltd (previously named Nuclear Sciences and Technology Services) and BNFL are thanked for funding this work. We are forever in debt to our colleague, the late Prof. Peter F. James, who was the inspiration behind this work and is sadly missed.

References

- [1] M.J. Larkin, Nucl. Energy 25 (6) (1986) 343–54.
- [2] J.A.C. Marples, Glass Technol. 29 (6) (1988) 230–47.

- [3] W. Lutze, in: W. Lutze, R.C. Ewing (Eds.), *Radioactive Waste Forms for the Future*, North-Holland, Amsterdam, 1988, pp. 1–159.
- [4] I.W. Donald, B.L. Metcalfe, R.N.J. Taylor, *J. Mater. Sci.* 32 (22) (1997) 5851–87.
- [5] M.I. Ojovan, W.E. Lee, *An Introduction to Nuclear Waste Immobilisation*, Elsevier Ltd, Oxford, 2005.
- [6] W.E. Lee, M.I. Ojovan, M.C. Stennett, N.C. Hyatt, *Adv. Appl. Ceram.* 105 (1) (2006) 3–12.
- [7] P.B. Rose, PhD thesis, University of Sheffield, Sheffield, UK, 2008.
- [8] G. Roth, S. Weisenburger, W. Grünwald, Y. Gauthier, in: *Proceedings of the 8th International Conference on Radioactive Waste Management and Environmental Remediation (ICEM'01, Bruges, Belgium)*, vol. 3, ASME, New York, 2002, pp. 1563–8.
- [9] Q. Yan, A.C. Buechele, S. Hu, E. Wang, S.S. Fu, *Ceram. Trans.* 61 (1995) 167–76.
- [10] B.-F. Zhu, D.E. Clark, L.L. Hench, G.G. Wicks, *J. Non-Cryst. Solids* 80 (1–3) (1986) 324–34.
- [11] S. Komarneni, R. Roy, D.M. Roy, *Nucl. Technol.* 62 (1983) 71–4.
- [12] M. Le Grand, PhD thesis, Université Paris 7 – Denis Diderot, Paris, France, 1999.
- [13] E. Schiewer, H. Rabe, S. Weisenburger, *Mater. Res. Soc. Symp. Proc.* 11 (1982) 289–97.
- [14] A.G. Blasewitz, BNWL-1401, Pacific Northwest Laboratory, Richland, WA, USA, 1970.
- [15] D. Caurant, O. Majérus, E. Fadel, M. Lenoir, C. Gervais, O. Pinet, *J. Am. Ceram. Soc.* 90 (3) (2007) 774–83.

- [16] A.K. Dé, B. Luckscheiter, W. Lutze, G. Malow, E. Schiewer, *Am. Ceram. Soc. Bull. (Ceram. Bull.)* 55 (5) (1976) 500–3.
- [17] A.R. Hall, J.T. Dalton, B. Hudson, J.A.C. Marples, in: *Management of Radioactive Wastes from the Nuclear Fuel Cycle, Proc. Symp.*, vol. 2, IAEA, Vienna, 1976, pp. 3–14.
- [18] C.P. Kaushik, R.K. Mishra, P. Sengupta, A. Kumar, D. Das, G.B. Kale, K. Raj, *J. Nucl. Mater.* 358 (2–3) (2006) 129–38.
- [19] K. Kawamura, J. Ohuchi, *Mater. Res. Soc. Symp. Proc.* 353 (1995) 87–93.
- [20] S. Morgan, PhD thesis, University of Sheffield, Sheffield, UK, 2005.
- [21] J.B. Morris, B.E. Chidley, in: *Management of Radioactive Wastes from the Nuclear Fuel Cycle, Proc. Symp.*, vol. 1, IAEA, Vienna, 1976, pp. 241–58.
- [22] R. Short, PhD thesis, University of Sheffield, Sheffield, UK, 2004.
- [23] G.K. Sullivan, M.H. Langowski, P. Hrma, *Ceram. Trans.* 61 (1995) 187–93.
- [24] J.V. Crum, J.D. Vienna, D.K. Peeler, I.A. Reamer, D.J. Pittman, *Ceram. Trans.* 132 (2002) 267–75.
- [25] J.E. Mendel, W.A. Ross, F.P. Roberts, R.P. Turcotte, Y.B. Katayama, J.H. Westsik Jr, in: *Management of Radioactive Wastes from the Nuclear Fuel Cycle, Proc. Symp.*, vol. 2, IAEA, Vienna, 1976, pp. 49–61.
- [26] H. Mitamura, T. Banba, T. Murakami, *Nucl. Chem. Waste Manag.* 6 (3–4) (1986) 223–31.
- [27] D.B. Spilman, L.L. Hench, D.E. Clark, *Nucl. Chem. Waste Manag.* 6 (2) (1986) 107–19.
- [28] H. Li, P. Hrma, J.D. Vienna, *Ceram. Trans.* 119 (2001) 237–45.
- [29] D. Manara, A. Grandjean, O. Pinet, J.L. Dussossoy, D.R. Neuville, *J. Non-Cryst. Solids* 353 (1) (2007) 12–23.

- [30] D.A. McKeown, I.S. Muller, H. Gan, I.L. Pegg, C.A. Kendziora, *J. Non-Cryst. Solids* 288 (1–3) (2001) 191–9.
- [31] I.L. Pegg, I. Joseph, in: C.H. Oh (Ed.), *Hazardous and Radioactive Waste Treatment Technologies Handbook*, CRC Press, Boca Raton, 2001, 4.2, pp. 1–27.
- [32] P. Sengupta, J. Mitra, G.B. Kale, *J. Nucl. Mater.* 350 (1) (2006) 66–73.
- [33] R.J. Short, R.J. Hand, N.C. Hyatt, G. Möbus, *J. Nucl. Mater.* 340 (2–3) (2005) 179–86.
- [34] J.D. Vienna, PhD thesis, Washington State University, Pullman, WA, USA, 2002.
- [35] P. Hrma, L.M. Bagaasen, A.E. Beck, T.M. Brouns, D.D. Caldwell, M.L. Elliott, J. Matyas, K.B.C. Minister, M.J. Schweiger, D.M. Strachan, B.P. Tinsley, G.W. Hollenberg, PNNL-15193, Pacific Northwest National Laboratory, Richland, WA, USA, 2005.
- [36] D.S. Kim, C.Z. Soderquist, J.P. Icenhower, B.P. McGrail, R.D. Scheele, B.K. McNamara, L.M. Bagaasen, M.J. Schweiger, J.V. Crum, D.J. Yeager, J. Matyáš, L.P. Darnell, H.T. Schaefer, A.T. Owen, A.E. Kozelisky, L.A. Snow, M.J. Steele, PNNL-15131, Pacific Northwest National Laboratory, Richland, WA, USA, 2005.
- [37] M.H. Langowski, J.G. Darab, P.A. Smith, PNNL-11052, Pacific Northwest National Laboratory, Richland, WA, USA, 1996.
- [38] A.V. Demin, M.I. Fedorova, Yu.I. Matyunin, *At. Energy (N. Y.)* 80 (3) (1996) 178–81.
- [39] L. Galois, G. Calas, G. Morin, S. Pugno, C. Fillet, *J. Mater. Res.* 13 (5) (1998) 1124–7.
- [40] W. Grünwald, G. Roth, W. Tobie, K. Weiß, S. Weisenburger, *Glass Technol.: Eur. J. Glass Sci. Technol., Part A* 49 (6) (2008) 266–78.

- [41] Ch. Krause, B. Luckscheiter, *J. Mater. Res.* 6 (12) (1991) 2535–46.
- [42] M.J. LaMont, P. Hrma, *Ceram. Trans.* 87 (1998) 343–8.
- [43] P. Izak, P. Hrma, B.W. Arey, T.J. Plaisted, *J. Non-Cryst. Solids* 289 (1–3) (2001) 17–29.
- [44] D.F. Bickford, A. Applewhite-Ramsey, C.M. Jantzen, K.G. Brown, *J. Am. Ceram. Soc.* 73 (10) (1990) 2896–902.
- [45] D.S. Goldman, D.W. Brite, *J. Am. Ceram. Soc.* 69 (5) (1986) 411–3.
- [46] C. Simonnet, A. Grandjean, *J. Non-Cryst. Solids* 351 (19–20) (2005) 1611–8.
- [47] D.E. Clark, L.L. Hench, *Nucl. Chem. Waste Manag.* 2 (2) (1981) 93–101.
- [48] P. Hrma, B.J. Riley, J.D. Vienna, *Ceram. Trans.* 143 (2003) 291–8.
- [49] D.-S. Kim, D.K. Peeler, P. Hrma, *Ceram. Trans.* 61 (1995) 177–85.
- [50] J.F. Sproull, S.L. Marra, C.M. Jantzen, *Mater. Res. Soc. Symp. Proc.* 333 (1994) 15–25.
- [51] D. Caurant, O. Majerus, P. Loiseau, I. Bardez, N. Baffier, J.L. Dussossoy, *J. Nucl. Mater.* 354 (1–3) (2006) 143–62.
- [52] H.J. Matzke, *Inorg. Chim. Acta* 94 (1–3) (1984) 142–3.
- [53] A. Quintas, O. Majérus, D. Caurant, J.-L. Dussossoy, P. Vermaut, *J. Am. Ceram. Soc.* 90 (3) (2007) 712–9.
- [54] F. Bart, J.L. Dussossoy, C. Fillet, *Mater. Res. Soc. Symp. Proc.* 663 (2001) 161–7.
- [55] L. Bouchet, A. Rivoallan, J.F. Milot, F. Bart, *Atalante 2000 Conference*, Avignon, France, 2000, P4-26.
- [56] P.K. Abraitis, PhD thesis, University of Manchester, Manchester, UK, 1999.
- [57] S.V. Raman, B.A. Scholes, A. Erickson, A.A. Zareba, *Ceram. Trans.* 143 (2003) 185–98.

- [58] A.C. Buechele, X. Feng, H. Gu, I.L. Pegg, *Mater. Res. Soc. Symp. Proc.* 176 (1990) 393–402.
- [59] N.C. Hyatt, K.J. Taylor, F.G.F. Gibb, W.E. Lee, *Glass Technol.* 45 (2) (2004) 68–70.
- [60] C.M. Jantzen, D.F. Bickford, D.G. Karraker, *Adv. Ceram.* 8 (1984) 30–8.
- [61] L. Kahl, *Nucl. Chem. Waste Manag.* 2 (2) (1981) 143–6.
- [62] D.-S. Kim, P. Hrma, D.E. Smith, M.J. Schweiger, *Ceram. Trans.* 39 (1994) 179–89.
- [63] B. Luckscheiter, M. Nesovic, *Waste Manag.* 16 (7) (1996) 571–8.
- [64] W. Lutze, J. Borchardt, A.K. Dé, in: G.J. McCarthy (Ed.), *Scientific Basis for Nuclear Waste Management I*, Plenum Press, New York, 1979, pp. 69–81.
- [65] Hj. Matzke, L. Kahl, J. Saidl, J.L. Routbort, *Adv. Ceram.* 8 (1984) 697–709.
- [66] O. Pinet, S. Mure, *J. Non-Cryst. Solids* 355 (3) (2009) 221–7.
- [67] S.K. Sundaram, J.M. Perez Jr, PNNL-13347, Pacific Northwest National Laboratory, Richland, WA, USA, 2000.
- [68] R.P. Turcotte, J.W. Wald, R.P. May, in: C.J.M. Northrup Jr (Ed.), *Scientific Basis for Nuclear Waste Management II*, Plenum Press, New York, 1980, pp. 141–6.
- [69] H. Mitamura, T. Murakami, T. Banba, *J. Nucl. Mater.* 136 (1) (1985) 104–16.
- [70] G. Roth, S. Weisenburger, *Nucl. Eng. Des.* 202 (2–3) (2000) 197–207.
- [71] P. Cheron, Ph. Chevalier, R. Do Quang, G. Tanguy, M. Sourrouille, S. Woignier, N. Senoo, T. Banba, K. Kuramoto, T. Yamaguchi, K. Shimizu, C. Fillet, N. Jacquet-Francillon, J. Godard, J.L. Dussossoy, F. Pacaud, J.G. Charbonnel, *Mater. Res. Soc. Symp. Proc.* 353 (1995) 55–62.
- [72] F. Pacaud, C. Fillet, N. Jacquet-Francillon, *Mater. Res. Soc. Symp. Proc.* 257 (1992) 161–7.

- [73] D.F. Bickford, C.M. Jantzen, *J. Non-Cryst. Solids* 84 (1–3) (1986) 299–307.
- [74] K.V.K. Rao, L. Iyengar, *Acta. Crystallogr., Sect. A: Cryst. Phys., Diffr., Theor. Gen. Crystallogr.* 25 (2) (1969) 302–3.
- [75] D.F. Bickford, C.M. Jantzen, *Mater. Res. Soc. Symp. Proc.* 26 (1984) 557–66.
- [76] H. Okamoto, *J. Phase Equilib.* 13 (1) (1992) 73–8.
- [77] H. Okamoto, *J. Phase Equilib.* 15 (3) (1994) 369.
- [78] H. Okamoto, *J. Phase Equilib.* 13 (1) (1992) 69–72.
- [79] A. Della Giusta, F. Princivalle, S. Carbonin, *Mineral. Petrol.* 37 (3–4) (1987) 315–21.
- [80] C.J. Capobianco, M.J. Drake, *Geochim. Cosmochim. Acta* 54 (3) (1990) 869–74.
- [81] P. Hrma, J.V. Crum, P.R. Brecht, L.R. Greenwood, B.W. Arey, H.D. Smith, *J. Nucl. Mater.* 345 (1) (2005) 31–40.
- [82] K.E. Sickafus, L. Minervini, R.W. Grimes, J.A. Valdez, M. Ishimaru, F. Li, K.J. McClellan, T. Hartmann, *Science* 289 (5480) (2000) 748–51.
- [83] A.C. Buechele, I.S. Muller, I.L. Pegg, C.-W. Kim, E. Yaschenko, *Ceram. Trans.* 61 (1995) 203–11.
- [84] I.S. Muller, A.C. Buechele, F. Perez-Cardenas, H. Gan, I.L. Pegg, *Mater. Res. Soc. Symp. Proc.* 556 (1999) 271–8.
- [85] P. Bouvier, E. Djuardo, G. Lucazeau, T. Le Bihan, *Phys. Rev. B: Condens. Matter Mater. Phys.* 62 (13) (2000) 8731–7.
- [86] T.P. O'Holleran, S.G. Johnson, P.C. Kong, B.A. Staples, *Ceram. Trans.* 87 (1998) 541–50.
- [87] M. Yashima, H. Arashi, M. Kakihana, M. Yoshimura, *J. Am. Ceram. Soc.* 77 (4) (1994) 1067–71.
- [88] W. Lutze, R.C. Ewing, *Ceram. Trans.* 61 (1995) 357–64.

- [89] N. Jacquet-Francillon, F. Pacaud, P. Queille, *Mater. Res. Soc. Symp. Proc.* 11 (1982) 249–59.
- [90] W.L. Gong, W. Lutze, R.C. Ewing, *J. Nucl. Mater.* 278 (1) (2000) 73–84.
- [91] A. Martínez-Arias, M. Fernández-García, V. Ballesteros, L.N. Salamanca, J.C. Conesa, C. Otero, J. Soria, *Langmuir* 15 (14) (1999) 4796–802.
- [92] R.D. Shannon, *Acta Crystallogr., Sect. A: Cryst. Phys., Diffr., Theor. Gen. Crystallogr.* 32 (5) (1976) 751–67.
- [93] M. Arbab, V.K. Marghussian, H. Sarpoolaky, M. Kord, *Ceram. Int.* 33 (6) (2007) 943–50.
- [94] C.M. Jantzen, K.G. Brown, J.B. Pickett, *Ceram. Trans.* 119 (2001) 271–80.
- [95] J.-H. Jean, T.-H. Kuan, T.K. Gupta, *J. Mater. Sci. Lett.* 14 (15) (1995) 1068–70.
- [96] B.J. Riley, P. Hrma, J. Rosario, J.D. Vienna, *Ceram. Trans.* 132 (2002) 257–65.
- [97] J.J. Pluth, J.V. Smith, J. Faber Jr, *J. Appl. Phys.* 57 (4) (1985) 1045–9.
- [98] D.R. Peacor, *Z. Kristallogr., Kristallgeom., Kristallphys., Kristallchem.* 138 (1973) 274–98.
- [99] I.P. Swainson, M.T. Dove, *Phys. Chem. Miner.* 22 (1) (1995) 61–5.
- [100] C.J. McConville, W.E. Lee, J.H. Sharp, *Br. Ceram. Trans.* 97 (4) (1998) 162–8.
- [101] K. Sun, L.M. Wang, R.C. Ewing, W.J. Weber, *Nucl. Instrum. Methods Phys. Res., Sect. B* 218 (2004) 368–74.
- [102] P.K. Abraitis, F.R. Livens, J.E. Monteith, J.S. Small, D.P. Trivedi, D.J. Vaughan, R.A. Wogelius, *Appl. Geochem.* 15 (9) (2000) 1399–416.
- [103] Aa. Barkatt, P.B. Macedo, W. Sousanpour, Al. Barkatt, M.A. Boroomand, C.F. Fisher, J.J. Shirron, P. Szoke, V.L. Rogers, *Nucl. Chem. Waste Manag.* 4 (2) (1983) 153–69.

- [104] D.E. Clark, C.A. Maurer, A.R. Jurgensen, L. Urwongse, Mater. Res. Soc. Symp. Proc. 11 (1982) 1–11.
- [105] R.M. Hazen, L.W. Finger, J.W.E. Mariathasan, J. Phys. Chem. Solids 46 (2) (1985) 253–63.
- [106] S.N. Achary, S.J. Patwe, M.D. Mathews, A.K. Tyagi, J. Phys. Chem. Solids 67 (4) (2006) 774–81.
- [107] A. Abdelouas, J.-L. Crovisier, W. Lutze, B. Grambow, J.-C. Dran, R. Müller, J. Nucl. Mater. 240 (2) (1997) 100–11.
- [108] W.L. Gong, L.M. Wang, R.C. Ewing, E. Vernaz, J.K. Bates, W.L. Ebert, J. Nucl. Mater. 254 (2–3) (1998) 249–65.
- [109] D. Savage, J.E. Robbins, R.J. Merriman, Mineral. Mag. 49 (351) (1985) 195–201.
- [110] D. Taylor, Trans. J. Br. Ceram. Soc. 83 (2) (1984) 32–7.
- [111] R.K. Mishra, P. Sengupta, C.P. Kaushik, A.K. Tyagi, G.B. Kale, K. Raj, J. Nucl. Mater. 360 (2) (2007) 143–50.
- [112] C.-W. Kim, I.S. Muller, A.C. Buechele, I.L. Pegg, P.B. Macedo, Mater. Res. Soc. Symp. Proc. 412 (1996) 149–56.
- [113] J.M. Marr, F.P. Glasser, Mineral. Mag. 43 (325) (1979) 171–3.
- [114] A.M. Shaikh, J. Indian Inst. Sci. 87 (2) (2007) 237–59.
- [115] D.A. McKeown, A.C. Buechele, H. Gan, I.L. Pegg, J. Non-Cryst. Solids 354 (27) (2008) 3142–51.
- [116] D.A. McKeown, I.S. Muller, A.C. Buechele, I.L. Pegg, C.A. Kendziora, C.R. Scales, Mater. Res. Soc. Symp. Proc. 556 (1999) 305–12.

Figure captions

Fig. 1. (a) BE SEM image of an as-cast sample displaying a compositionally homogeneous glass matrix (Type I microstructure). (b) BE SEM image of an as-cast sample displaying a compositionally inhomogeneous glass matrix with compositional ‘banding’ and ‘reprecipitated calcine’ (Type II microstructure).

Fig. 2. (a) BE SEM image of an as-cast sample displaying a Type II microstructure with compositional ‘banding’. The location and direction of an EDX line scan is indicated (starts bottom left and stops top right). (b) EDX line scan traces from the location and in the direction indicated in (a). Traces are offset for clarity.

Fig. 3. XRD traces of as-cast samples. RuO₂ was also identified (but not labelled) in trace (b). Traces are offset for clarity.

Fig. 4. (a) BE SEM image of acicular RuO₂ crystals in an as-cast sample. (b) BF TEM micrograph of an acicular RuO₂ crystal contacting other RuO₂ crystals in an as-cast sample. (c) BE SEM image of an uncommonly large acicular RuO₂ crystal with cracks emanating from it in an as-cast sample. The origin and tip of cracks are arrowed. (d) BE SEM image of an uncommon globular Ru metal inclusion in an as-cast sample.

Fig. 5. (a) BE SEM image of a spheroidal Pd–Te alloy inclusion in an as-cast sample. (b) SE SEM image of a globular Pd–Te alloy inclusion in an as-cast sample.

Fig. 6. (a) SE SEM image of a faceted $(\text{Cr,Fe,Ni,Ru})_3\text{O}_4$ crystal in an as-cast sample. (b) SE SEM image of a cluster of faceted $(\text{Cr,Fe,Ni,Ru})_3\text{O}_4$ crystals in an as-cast sample.

Fig. 7. (a) BE SEM image of globular agglomerates of $\text{Zr}_{1-x-y}\text{Ce}_x\text{Gd}_y\text{O}_{2-0.5y}$ nanocrystals (light grey) and bubbles (black) in an as-cast sample. (b) BF TEM micrograph of $\text{Zr}_{1-x-y}\text{Ce}_x\text{Gd}_y\text{O}_{2-0.5y}$ nanocrystals in an as-cast sample. The dark speckled contrast features approximately 3–17 nm in size are nanocrystals. (c) Partial electron diffraction pattern from the $\text{Zr}_{1-x-y}\text{Ce}_x\text{Gd}_y\text{O}_{2-0.5y}$ nanocrystals in (b). The ring pattern is due to the nanocrystals being randomly oriented.

Fig. 8. BE SEM image of hexagonal lanthanoid (Nd,Gd,La,Ce) silicate crystals (light grey), globular agglomerates of $\text{Zr}_{1-x-y}\text{Ce}_x\text{Gd}_y\text{O}_{2-0.5y}$ nanocrystals (grey), bubbles (black) and cracking in an as-cast sample. Image is of the interior of the ‘reprecipitated calcine’ in Fig. 1(b).

Fig. 9. (a) SE and (b) BE SEM images of a heat treated sample displaying extensive crystallisation (Type A microstructure). (c) SE SEM image of a heat treated sample displaying extensive sample cracking (Type A microstructure). (d) BE SEM image of a heat treated sample displaying ‘banded’ crystallisation (Type B microstructure).

Fig. 10. XRD traces of heat treated samples. RuO_2 was also identified (but not labelled) in trace (b). Traces are offset for clarity.

Fig. 11. (a) BE SEM image of a dendritic SiO_2 (α -cristobalite) crystal in a heat treated sample. (b) SE SEM image of extensive cracking in and around dendritic α -cristobalite crystals in a heat treated sample.

Fig. 12. BE SEM image of a dendritic $(\text{Na},\text{Sr},\text{Nd},\text{La})\text{MoO}_4$ crystal which has nucleated and grown on a RuO_2 crystal and displays internal cracking in a heat treated sample. The origin and tip of cracks are arrowed.

Fig. 13. (a) BF TEM micrograph of spheroidal $\text{Ce}_{1-x-y}\text{Zr}_x\text{Gd}_y\text{O}_{2-0.5y}$ crystals displaying crystal twinning in a heat treated sample. (b) BF TEM micrograph of a cluster of acicular Ni-rich crystals nucleated and grown on a RuO_2 crystal in a heat treated sample.

Fig. 14. (a) BE SEM image of acicular/platy lanthanoid $(\text{Nd},\text{Gd},\text{La},\text{Ce})$ silicate crystals (white) in a heat treated sample. (b) SE SEM image of acicular $\text{LiNaZrSi}_6\text{O}_{15}$ (zektzerite) crystals (grey), lanthanoid $(\text{Nd},\text{Gd},\text{La},\text{Ce})$ silicate crystals (light grey, penetrated by zektzerite crystals) and cracking in a heat treated sample.

Fig. 15. (a) SE SEM image of acicular $\text{LiNaZrSi}_6\text{O}_{15}$ (zektzerite) crystals (grey) and cracking in a heat treated sample. The location and direction of an EDX line scan is indicated, it starts on a $\text{Ce}_{1-x-y}\text{Zr}_x\text{Gd}_y\text{O}_{2-0.5y}$ crystal (light grey, top left) and stops on a lanthanoid $(\text{Nd},\text{Gd},\text{La},\text{Ce})$ silicate crystal (light grey, bottom right). (b) EDX line scan traces from the location and in the direction indicated in (a). Traces are offset for clarity.

Tables

Table 1

Chemical composition of Oxide glass

Component	wt%	mol%	Component	wt%	mol%
Al ₂ O ₃	0.60	0.40	Nd ₂ O ₃	2.44	0.50
B ₂ O ₃	18.14	17.79	NiO	0.46	0.42
BaO	0.57	0.25	P ₂ O ₅	0.11	0.05
CaO	0.02	0.02	PdO	0.52	0.29
CeO ₂	1.33	0.53	Pr ₆ O ₁₁	0.75	0.05
Cr ₂ O ₃	0.22	0.10	RuO ₂	1.02	0.52
Cs ₂ O	1.32	0.32	SO ₃	0.02	0.02
Fe ₂ O ₃	0.58	0.25	SiO ₂	49.19	55.90
Gd ₂ O ₃	2.81	0.53	Sm ₂ O ₃	0.41	0.08
HfO ₂	0.04	0.01	SrO	0.48	0.32
K ₂ O	0.05	0.04	TeO ₂	0.24	0.10
La ₂ O ₃	0.69	0.14	TiO ₂	0.02	0.02
Li ₂ O	3.88	8.87	Y ₂ O ₃	0.19	0.06
MgO	0.01	0.02	ZrO ₂	2.25	1.25
MoO ₃	2.67	1.27			
Na ₂ O	8.97	9.88	Total	100.00	100.00

Table 2

Waste loading (WL), molar mass (M), density (ρ), molar volume (V_m) and glass transition temperature (T_g) of unannealed as-cast Oxide glass

WL (wt%/mol%)	M (g mol ⁻¹)	ρ (g cm ⁻³)	V_m (cm ³ mol ⁻¹)	T_g (°C)
19.82/7.56	68.29	2.73(1) ^a	25.0	498(5) ^b

^a Figure in parentheses is two standard deviations from the mean.

^b Figure in parentheses is the estimated error.

Table 3

Mean linear (α_l) and volumetric (α_V) thermal expansion coefficients (TECs) of borosilicate HLW glasses and relevant crystal phases^a over the specified temperature ranges

	Temperature range (°C)	a ($\times 10^{-6} \text{ K}^{-1}$)	α_V ($\times 10^{-6} \text{ K}^{-1}$)	Reference(s)
Borosilicate HLW glasses	RT ^b – T_g	8.0–10.0	24.0–30.0	[3,4]
Ruthenium dioxide (RuO ₂)	30–361	$a = 9.7$ $c = -2.6$	16.8	[74]
	361–608	$a = 13.0$ $c = -3.8$	22.3	
Cristobalite (SiO ₂)	23–200 ^c	$a = 19.1$ $c = 34.2$	72.7	[97]
	(α -cristobalite)			
	200–300	$a = 112$ $c = 234$	465	[97–99]
	(α – β phase transition region)			
Powellite (CaMoO ₄)	25–300	$a = 11.7$ $c = 19.3$	42.9	[106]
	300–600	$a = 13.1$ $c = 21.7$	48.2	
Zektzerite (LiNaZrSi ₆ O ₁₅)	12–420	$a = 4.3$ $b = 3.1$ $c = 4.8$	12.2	[113]
	420–630	$a = 6.3$ $b = 6.0$ $c = 7.5$	19.9	

^a Isostructural crystal phases of different chemical composition may have different TECs.

^b Room temperature.

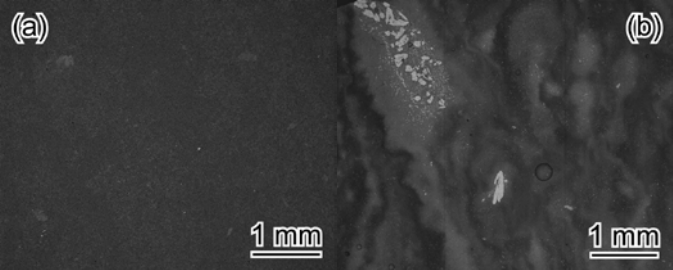
^c Also specified as 20–200 °C in the same reference, which would give mean TECs (α) for a , c and V of 18.8, 33.6 and $71.4 \times 10^{-6} \text{ K}^{-1}$ respectively.

(a)

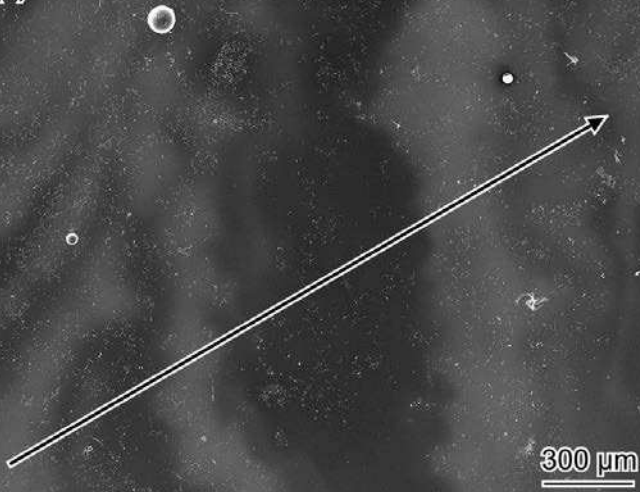
1 mm

(b)

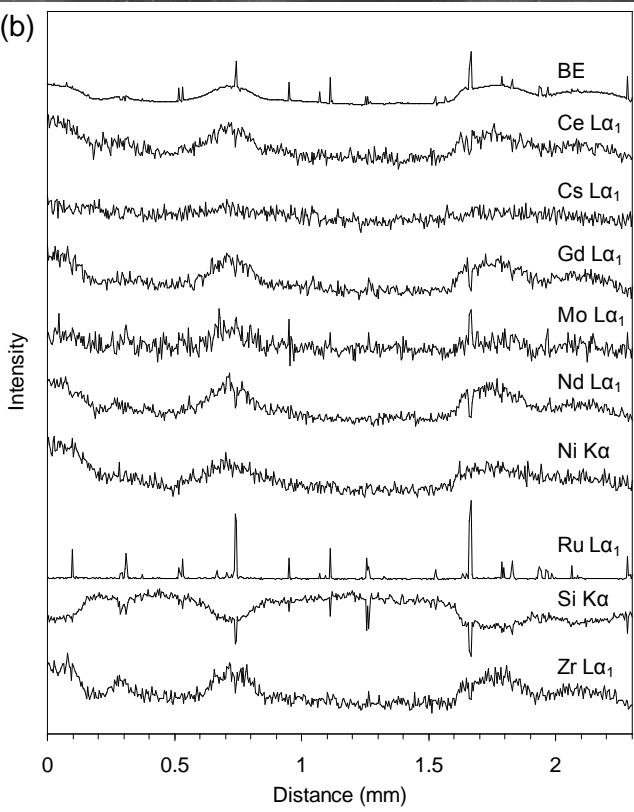
1 mm

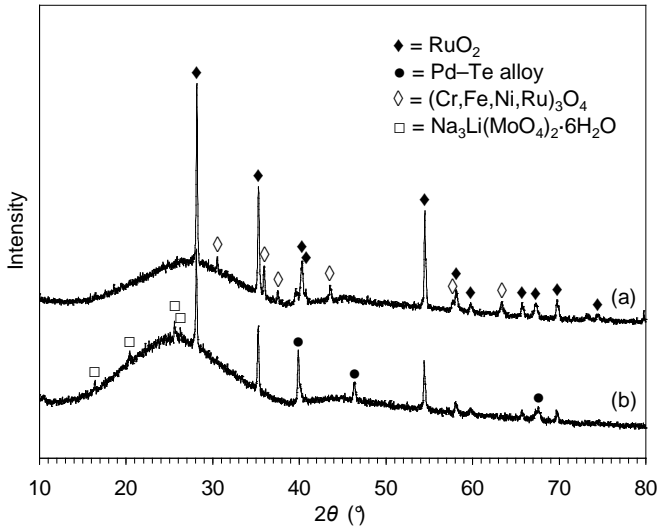


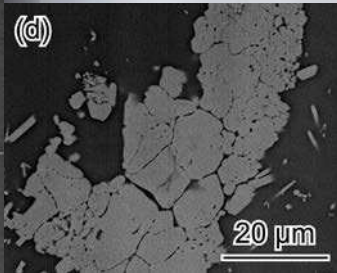
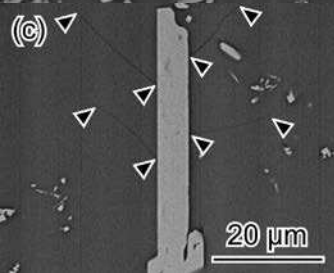
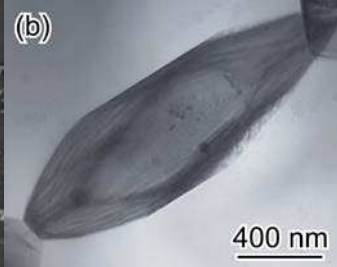
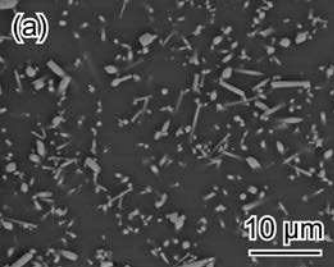
(a)



(b)







(a)



5 μm

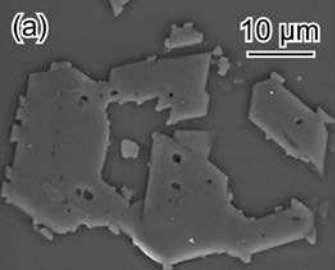
(b)



20 μm

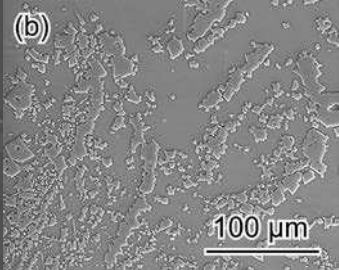
(a)

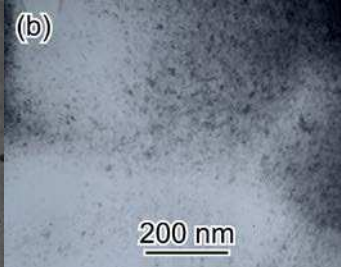
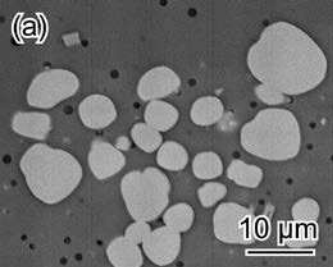
10 μm

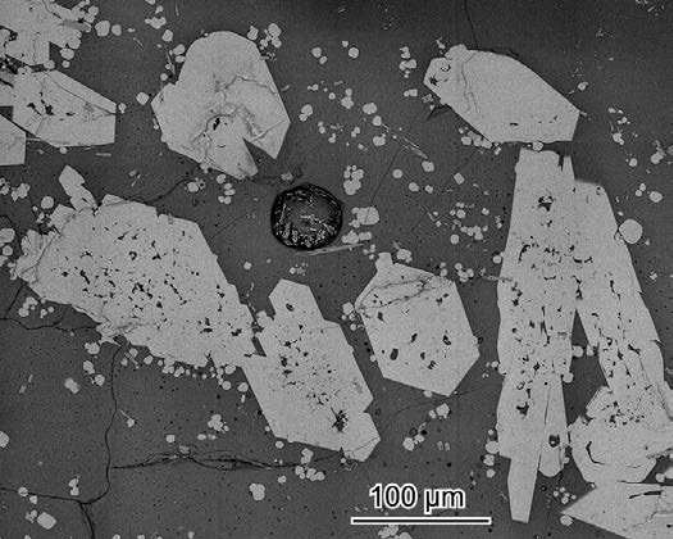


(b)

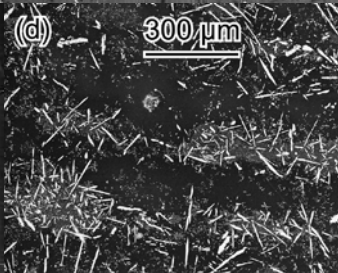
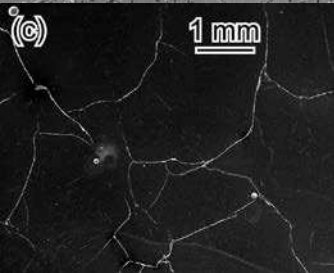
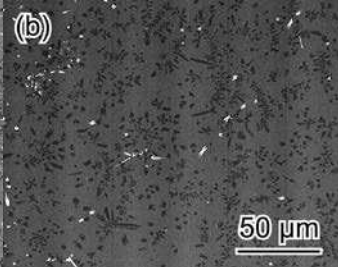
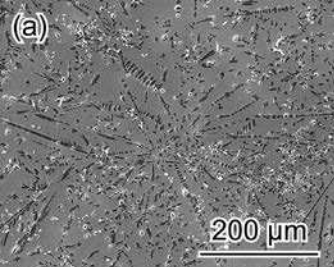
100 μm

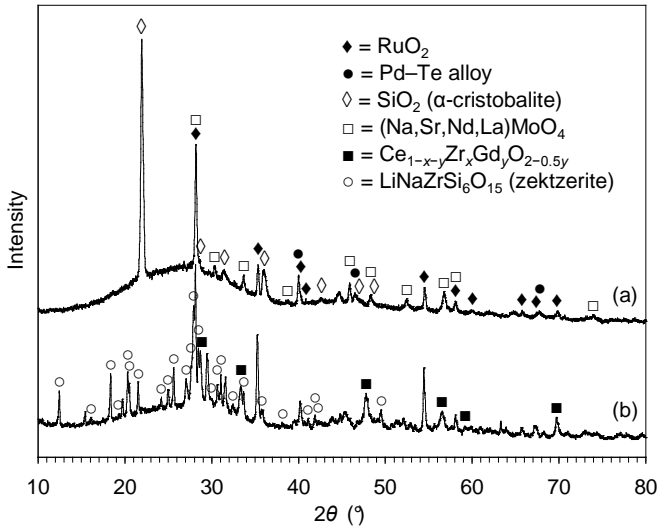




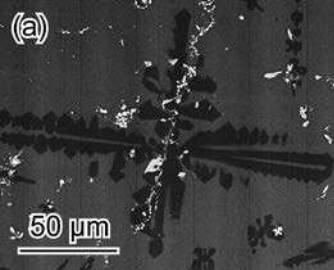


100 μm

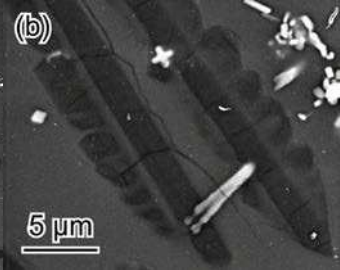


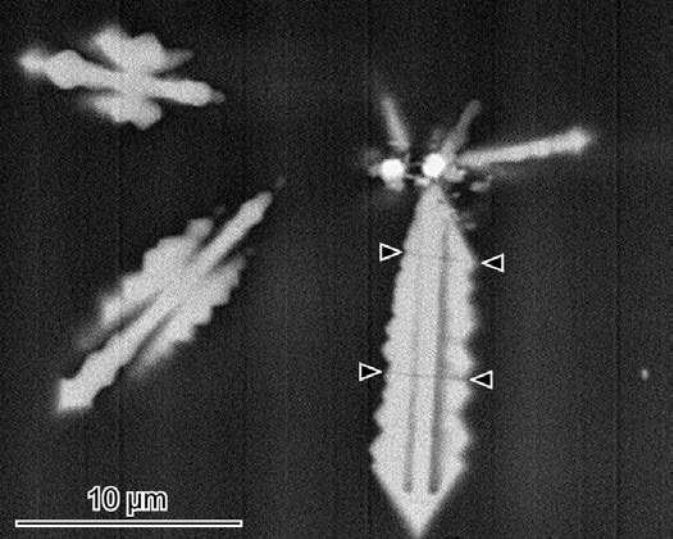


(a)



(b)

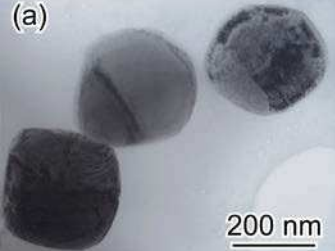




10 μm

This is a grayscale micrograph of a biological specimen, likely a larva or insect. The specimen is oriented vertically, with its head at the top. The head region shows two bright, circular eyes. The body is elongated and tapers towards the bottom. There are four white triangles pointing to specific features on the body: two on the left side and two on the right side, positioned roughly in the middle and lower-middle sections. A horizontal scale bar is located in the bottom left corner, labeled '10 μm'. The background is dark and textured.

(a)



(b)

